www.cadanda.com
Computer-Aided Design AND APPLICATIONS

Minimization of Bone Removal through Optimal Humeral Implant Alignment in Total Elbow Arthroplasty

Alexander J. Heroux[1], O. Remus Tutunea-Fatan[2], Shaun P. Salisbury[3] and Ahmad Barari[4]

[1]Western University, aheroux@uwo.ca
[2]Western University, rtutunea@eng.uwo.ca
[3]Western University, ssalisb2@uwo.ca
[4]University of Ontario Institute of Technology, ahmad.barari@uoit.ca

ABSTRACT

Total elbow arthroplasty (TEA) represents one of the surgical procedures performed on the upper limb in order to replace the diseased joint with a prosthetic device. According to current surgical standards, TEA is carried out with little information on the amount of bone to be removed in order to allow the installation of the implant within the medullary canal of the humerus. To address this, the present study proposes a numerical technique capable to estimate both the amount and location of the bone to be removed from the canal. As a first step, the developed method entails the extraction of the outer and inner contours of the bone based on the raw CT data. Then, global optimization search built on a gradient-based solver was used to identify the implant posture which minimizes the total interference amount as quantified across the entire length of the analyzed humeral specimen. After the proposed approach was tested on three different specimens and compared with a computationally-intensive baseline, clinically-relevant information was extracted in an attempt to provide the surgeons with more effective means to decide on the location and the amount of bone to be removed.

Keywords: total elbow arthroplasty, bone removal, implant insertion, flexion-extension (FE) axis alignment/malalignment, outer and inner bone contours, point datasets, implant posture, total interference minimization, global optimization search, clinically-relevant data.

1. INTRODUCTION

Total elbow arthroplasty (TEA) is a surgical procedure aiming to address and/or correct various pathological conditions associated with rheumatoid arthritis, elbow joint injuries, elbow joint instability, and severe joint pain. The primary goal of the procedure is to replace one of the major articulations of the upper limb with a prosthetic device aiming to restore, to the highest degree, most of the lost functionality of its native counterpart. Since the overall incidence of TEA is relatively low compared to that of other joint arthroplasties, most orthopaedic surgeons tend to have insufficient exposure to the procedure and this in turn translates into their inadequate familiarity and proficiency with the process. As such, TEA patients often have to return for subsequent revision surgeries caused by the failure associated with the aseptic loosening of their implants [5,7,8,10,12].

According to the current standards for TEA, after the initial preparatory stages used to uncover the native articulation and then to remove the diseased/afflicted portions of the bone, the prosthetic replacement of the joint is installed between the humeral, ulnar and radial ends that are adjacent to the joint. This is performed by inserting the three stems of the implant into the medullary canals of the corresponding bones (Fig. 1), a step whose primary goal is to ensure a maximum degree of overlap between the native and prosthetic flexion-extension axes of the elbow.

As illustrated in Fig. 2a, the vast majority of models adopted by the clinicians tend to define the FE axis of the elbow – in a somewhat axiomatic manner - as the theoretical line joining the center of the spherical shaped capitellum with the center of the spool shaped trochlear sulcus [1,2,15–18,20,21,23]. Since capitellum and trochlea sulcus are acknowledged as two of the most important anatomical features of the distal humerus geometry, the humeral spool was designed in such a way to mimic them as close as possible

Computer-Aided Design & Applications, 11(4), 2014, 478–492, http://dx.doi.org/10.1080/16864360.2014.881192

Taylor & Francis

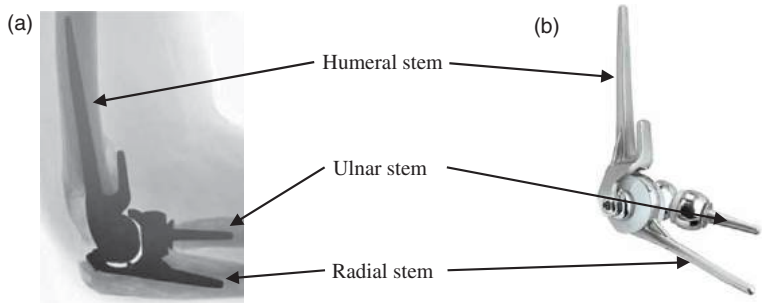

Fig. 1: Total elbow arthroplasty: a) postoperative lateral radiograph of the right elbow, and b) Tournier Latitude implant design.

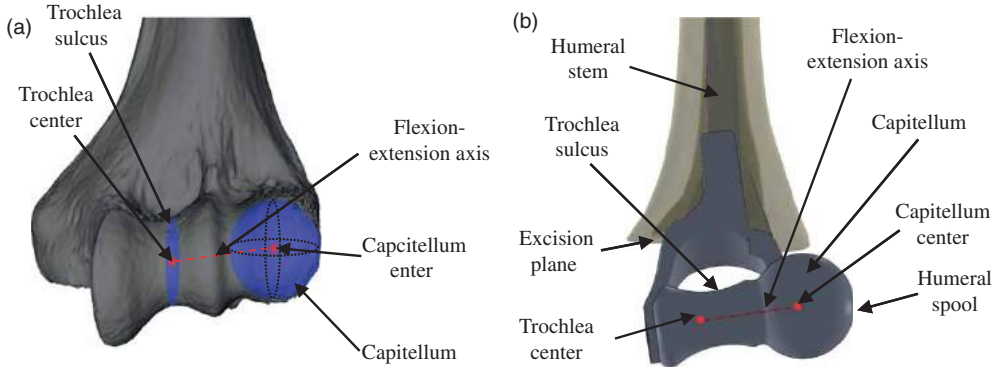

Fig. 2: Significant anatomical features of the distal humerus: a) native geometry, and b) prosthetic replica.

(Fig. 2b). Furthermore, many TEAs require the excision of the distal portion of the humerus in order to allow an appropriate insertion of the implant within the endosteal canal.

As it can be inferred, most of the implant installation challenges are related to the humeral link, and they are caused by the large length of the stem to be inserted and then cemented within the canal. Various combinations of broaches and/or reamers are used to enlarge the canal in order to facilitate implant insertion which is often impossible otherwise. The amount of bone to be removed varies from one individual to the other since it is strongly dependent upon the local anatomy of articulation to be replaced as well as the size of the implant to be used [3,19]. Given that elbow implants are generally produced in three to four standard sizes ranging from small to extra large [18], the probability of an ideal match between the available sizes and humeral geometry is relatively small in current clinical practice. Obviously, while large implants would be generally preferable for load transfer and fixation purposes, they tend to be difficult to insert due to the convoluted shape of the medullary canal. Conversely, smaller stems/implants are easier to install but they are characterized by lower dynamic indices. However, regardless of the scenario, the amount of cortical bone to be removed should be minimized at all costs in order to avoid: i) the extensive use of bone cement, which often leads to non-ideal loading conditions of the implant, and ii) substantial thinning and/or penetration of the cortical wall of the humerus [4,25]. Appropriate measures have to be taken to limit the amount of malalignment between the native and prosthetic FE axes of the elbow in order to warrant the long term success of the surgical procedure and thereby improve the overall patient outcomes and quality of life.

In the current clinical practice, most of the canal enlargement operations rely heavily on the expertise of the surgeon performing the TEA procedure. Both reaming and broaching of the humeral canal are typically performed in a “blind” or “semi-blind” manner due to the lack of intraoperative means to visualize the instantaneous location of the contact between the cutting tool and bone. Furthermore, since the anatomical diversity of the humeral geometry makes each implantation procedure unique, it is not uncommon that canal enlargement operations pose significant difficulties even to experienced surgical professionals.

To address this, the current study proposes a numerical technique capable to indicate the location of the minimal amount of cortical bone to be removed in order to allow a controlled/limited amount of malalignment between the native and prosthetic FE axes of the elbow joint. To increase the clinical relevance of the proposed approach in the surgical preoperative context, valid CT data acquired for clinical purposes was used as a primary input. The developed approach is comprised of two major steps: i) generation of unequivocal discrete point-based

representations of cortical bone contours from automatically segmented polygonal meshes from CT scans of the humerus; and ii) nonlinear optimization aiming to minimize the amount of bone removed while limiting the maximum amount of malalignment permitted between the native and prosthetic FE axes of the analyzed joint.

2. POINT-BASED REPRESENTATIONS OF BONE CONTOURS

The unequivocal identification of point-based representations for outer and inner boundaries of the cortical wall is essential for determining the relative position between implant and humeral points. In this regard, each of the implant points could occupy three distinct positions with respect to the bone: 1) within inner contour (*i.e.* inside of medullary canal, non-interfering condition), 2) between inner and outer contours (*i.e.* in interference condition), and 3) outside of outer contour (*i.e.* in penetration condition).

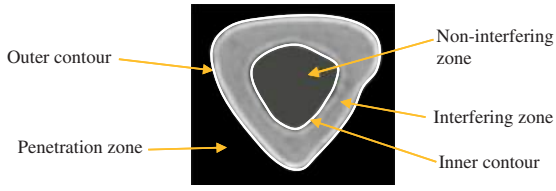

Fig. 3: Relative positioning options for implant points with respect to bone.

2.1. Preprocessing of Raw Point-based Input Datasets

The data constituting the primary input for the developed technique was prepared through a method routinely used by researchers in biomechanics to prepare 3D polygonal mesh models of the analyzed skeletal geometry. During this procedure, the stack of raw 2D data acquired by the CT scanner (Fig. 4a) is initially reconstructed into 3D voxel-based format that can be visualized with a specific volume rendering method (Fig. 4b). Then, in a second conversion step, the 3D voxelized representation is further processed to a polygonal mesh (Fig. 4c) format through a standard technique; for instance, marching cubes algorithm [13]. In this study, all investigated humeral specimens were converted through this technique to a commonly used mesh format called VTK; which constitutes the core of the Visualization Toolkit [11]. While a variety of software tools is available to complete these tasks, the present study relied on the latest version of Slicer3D freeware, in which segmentation parameters were set according to prior studies [20]. Once the VTK mesh data was created, only its vertices were retained for further processing. As Fig. 4c suggests, a certain amount of triangular mesh vertices are generally positioned between the original CT scan planes. In order to minimize the amount of information loss caused by their elimination, all of the "vertex outliers" were projected/shifted to the closest CT plane based on their relative position with respect to mid-voxel plane.

Figure 5 shows a sample comparison between the original raw CT data and its corresponding points created at the end of the preprocessing phase to serve as input for cortical bone boundaries identification to be detailed throughout the next sections. As the presented sample suggests, most of the contour identification challenges are caused by the presence of irregular and randomly distributed "islands" in the preprocessed data caused either by bone defects/voids and/or other imaging artifacts due to the unintentional segmentation of the soft tissue. While a more application-oriented segmentation could potentially eliminate most of the soft tissue contours, relatively little can be done about the innate bone defects whose presence hinders an adequate identification of the three main zones outlined in Fig. 3 which is a critical step towards the computation of the interference amount experienced for a certain implant posture.

2.2. Nearest Neighbor-based Identification of Outer Bone Contours

A quick but effective visual/qualitative analysis of the raw point-based dataset acquired suggests that preprocessing the distances between consecutive points on outer bone boundary are always larger than those between outer and inner contour points (Fig. 5b). This can be interpreted as a consequence of different point density characteristics to marginal and internal zones of the cortical bone. With this observation in mind, outer bone contours have been determined by means of nearest neighbor (NN) approach which aims for the point that has the smallest Euclidian distance with respect to the currently analyzed location. To increase computational speed by avoiding unnecessary distance calculations, Delaunay triangulation ($\mathcal{DT}$) was first applied on the planar subset of data points analyzed ($\mathcal{D}$). This technique was used to speculate one of fundamental properties of $\mathcal{DT}$, namely that NN graph is one of its subsets. With this transformation, the raw unsorted and thus "amorphous" set of points $\mathcal{D}$ is being converted into an organized structure that is characteristic to Delaunay-type data (Fig. 6a).

In other words, if $\mathrm{P}^{\mathrm{curr}} \in D$ is the current point identified on the outer contour $\mathcal{O}_{\mathrm{C}} \subset \mathcal{D}(\mathrm{P}^{\mathrm{curr}} \in \mathcal{O}_{\mathrm{C}})$, then the next point of the outer bone boundary ($\mathrm{P}^{\mathrm{next}} \in \mathcal{DT}(D)$ and $\mathrm{P}^{\mathrm{next}} \in \mathcal{O}_{\mathrm{C}}$) has to obey the following:

$$\begin{aligned} \mathrm{P}^{\mathrm{next}} &= \{\mathrm{P}_m^{\mathrm{cand}} \in \mathcal{DT}(\mathcal{D}) \,\big|\, |\mathbf{P}_{\mathrm{P}_m^{\mathrm{cand}}} - \mathbf{P}_{\mathrm{P}^{\mathrm{curr}}}| \\ &= \min_{\forall j \le n}(|\mathbf{P}_{\mathrm{P}_j^{\mathrm{cand}}} - \mathbf{P}_{\mathrm{P}^{\mathrm{curr}}}|), j \in \mathbb{N}\} \end{aligned} \quad (1)$$

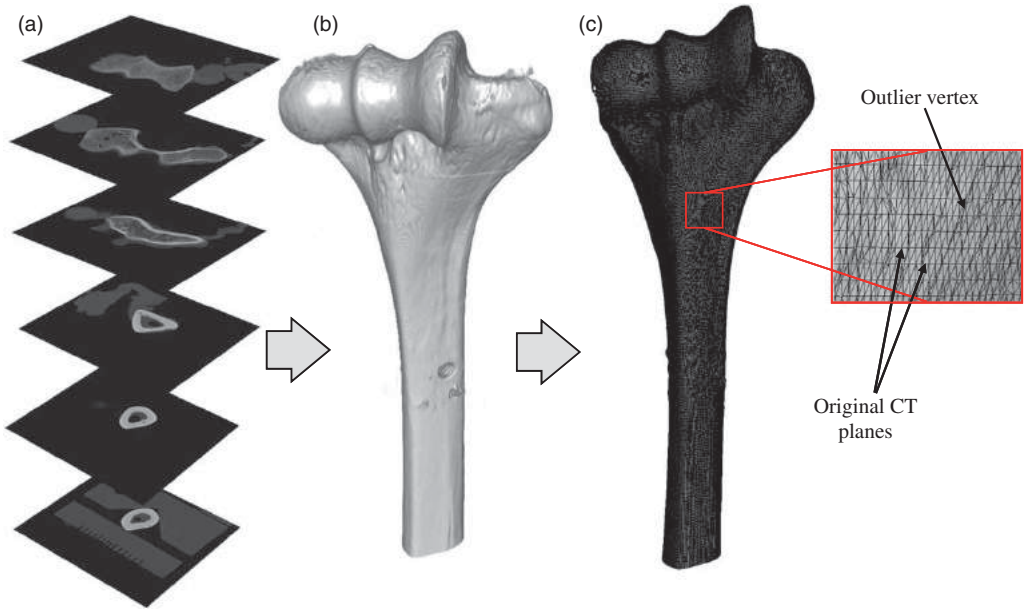

Fig. 4: CT to polygonal mesh conversion of data for humeral specimens: a) stack of raw CT slices, b) rendered humeral volume, and c) triangular mesh generation.

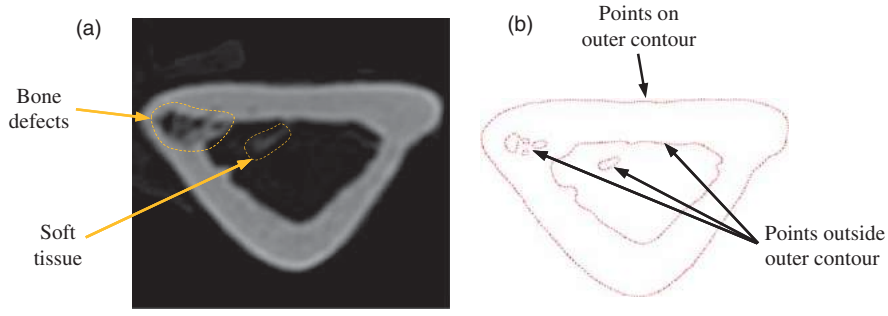

Fig. 5: Correspondence between original CT and preprocessed data: a) original CT slice, and b) extracted mesh vertices.

where P_j^{cand} are all n candidates neighboring triangulation vertices for the analyzed current point P^{curr} ($P^{curr} \in \mathcal{DT}(\mathcal{D})$) as shown in Fig. 6b. Once P^{next} is been determined, the location of P^{curr} is updated to P^{next} and then the old P^{curr} is deleted to force the advancement along outer contour vertices. Obviously, the identification of outer contour points will stop once the point used to initialize the NN search – typically selected at min(X) location – described above becomes equivalent with P^{next}. The iterative applications of this technique on all preprocessed CT slices will generate an ordered and clean representation for outer boundaries of the investigated humeral specimen (Fig. 6c).

2.3. Binning-based Identification of Inner Bone Contours

Despite of its robustness for outer boundaries, NN strategy failed to provide appropriate results for the more complex and convoluted geometry of the endosteal canal that often encompasses distanced regions of grouped points surrounding various bone defects and/or imaging artifacts as illustrated in Fig. 5a. Although various combinations of NN techniques were tested, none of them seemed capable to identify the inner bone contour in a manner that is consistent with an intuitive user-driven selection (Fig 7a).

It is perhaps important to note here the underlying assumption behind the proposed inner bone contour is that only solid (e.g. 100% nonporous) cortical bone will be tested in this study for interference with implant geometry. The logical consequence of this assumption is that porous/trabecular (e.g. with voids or bone defects) zones will be assigned a zero stiffness, in a sense that if the inserted implant stem will come in contact with them, they will be crushed and thus eliminated. Obviously, while an inherent degree of subjectivity is associated with this hypothesis, it is believed that this represents an acceptable simplification of the investigated problem.

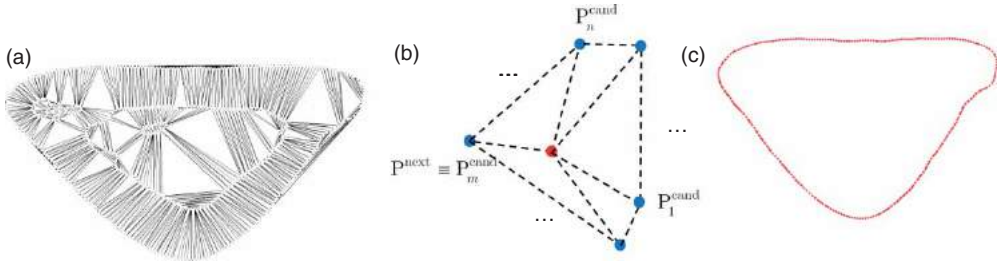

Fig. 6: Determination of point-based outer contours: a) Delaunay triangulation, b) nearest neighbor, and c) extracted final outer contour.

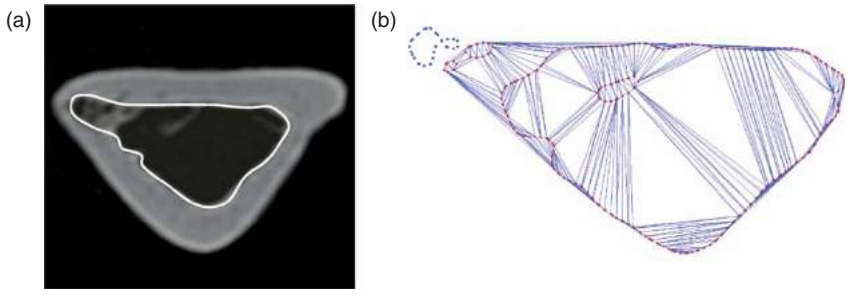

Fig. 7: Expected and actual results for inner contours identified with nearest neighbor strategy: a) user-selected inner contour, b) incorrect "island-trapped" inner contour.

The most common cause of failure for NN approach was related to "trapping" of the search to one of the regionalized "islands" that are often present in the context of medullary canal walls. While from a theoretical standpoint, this issue could be solved through an appropriate merging of the previously identified regions/islands of point datasets, the actual implementation was found to be inefficient in case of high variability exhibited by inner contour data.

To remedy this issue, a completely different route was taken to extract the points on the inner bone contour ($\mathcal{I}_C \subset \mathcal{D}$). Essentially, all points that were left out after the elimination of outer contour points from the preprocessed planar datasets (Fig. 5b) were divided into n_B "bins" ($\mathcal{B}$) of equal size as measured along Xdirection (Fig. 8a):

$$\Delta X_{\mathcal{B}} = \frac{\Delta X_{max}}{n_{\mathcal{B}}} = \frac{\max_{I_C}(X) - \min_{I_C}(X)}{n_{\mathcal{B}}} \tag{2}$$

In the current approach, the only criterion used to control the size of the bins and implicitly their number was chosen to be the minimum number of points in each bin. Heuristic searches performed with this technique on multiple humeral specimens have indicated that each bin should contain at least three points in it in order for this approach to work:

$$\text{count}_{\forall i \le n_B}(\text{P}) \ge 3 | \text{P} \in \mathcal{B}_i,\ i \in \mathbb{N} \tag{3}$$

where the condition $\text{P} \in \mathcal{B}_i$ is equivalent to:

$$\min_{\mathcal{B}_i}(X) \le X_{\text{P}} \le \max_{\mathcal{B}_i}(X),\ \forall i \le n_{\mathcal{B}},\ i \in \mathbb{N} \tag{4}$$

It is relatively easy to infer that the enforcement of the condition detailed in Eq. (3) generally leads to slight decreases in the number of bins as initially estimated with Eq. (2). However, as Fig. 8b shows, a minimum number of two points in each bin does not represent a feasible option since unexpected jumps in inner contour might occur after the next processing steps are performed. The explanation of this phenomenon resides in the technique used to select inner contour points combined with their intrinsic density/spacing within the preprocessed data. Essentially, the determination of inner contour points relies on the identification of points that are characterized by maximum/minimum Y coordinates in each of the previously identified bins:

$$\begin{aligned} \text{P}_{I_C} = \{\text{P} \in \mathcal{D} | Y_{\text{P}} = \max_{\mathcal{B}_i}(Y) \text{ or} \\ Y_{\text{P}} = \min_{\mathcal{B}_i}(Y),\ \forall i \le n_{\mathcal{B}},\ i \in \mathbb{N}\} \end{aligned} \tag{5}$$

When bins are only required to include a minimum of two points, they can be both located on the same "upper" or "lower" portion of the bone contour, such that unexpected variations of the boundary – like the one depicted in Fig. 8b – might occur. In the particular case shown in this figure, the jump was caused by the lack of points in the "upper" portion of the contour, *i.e.* the ones satisfying $\min_{\mathcal{B}_i}(Y)$ or $\max_{\mathcal{B}_i}(Y)$ conditions. By contrast, when minimum three points/bin are enforced, the inner contour is correctly detected (Fig. 8c). Further increases of the minimum number of points per bin will also yield acceptable contours

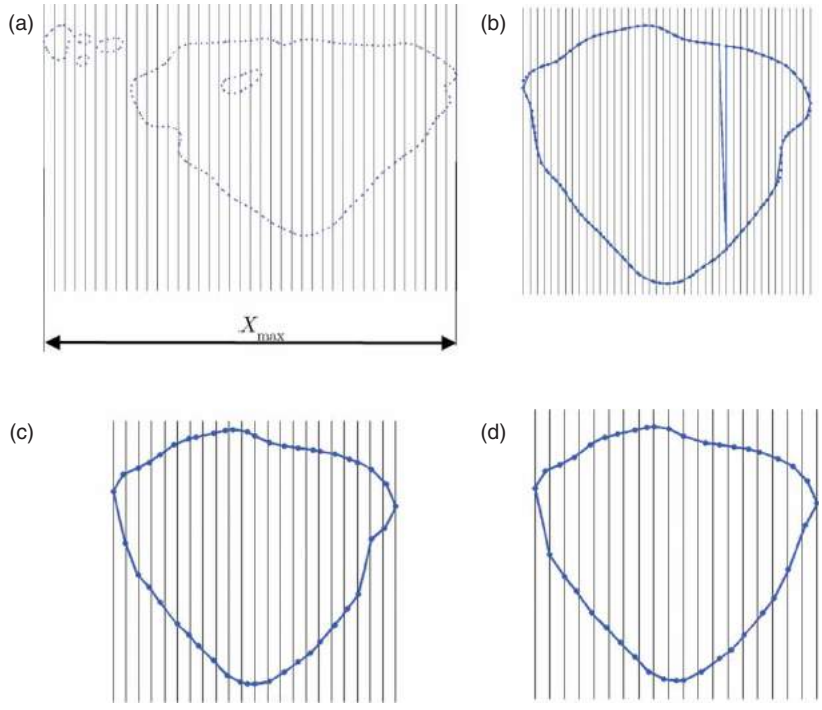

Fig. 8: Determination of appropriate bin size: a) initial estimation of even-sized bins, b) erroneous inner contour determination for a minimum of two points/bin, c) corrected inner profile for a minimum of three points/bin, and d) extracted inner contour points for minimum four points/bin.

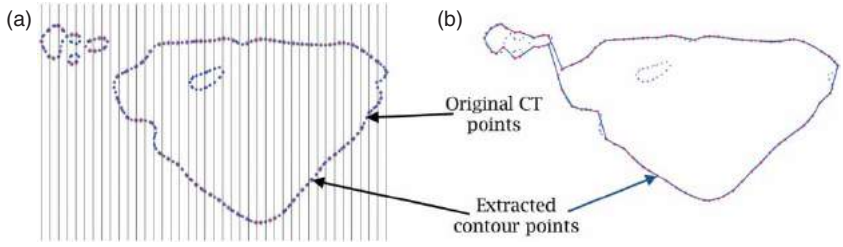

Fig. 9: Determination of point-based inner contours: a) selection of contour points, and b) extracted final inner contour.

(Fig. 8d), but points are more spaced apart and thus will capture less accurate details of the inner boundary.

Once all points meeting this condition have been located (Fig. 9a), the algorithm generates the inner canal contour simply by joining in an X-ordered manner all points with identical attributes ($\min_{\mathcal{B}_i}(Y)$ or $\max_{\mathcal{B}_i}(Y)$) to be followed by final interconnections between the two categories mentioned that are always distinctively positioned either in the upper or the lower zone of the analyzed boundary. These interconnections are always located around the extreme X points ($\min_{\mathcal{B}_i}(Y)$ and $\max_{\mathcal{B}_i}(Y)$) for each of the analyzed slices. Figure 9b illustrates the typical result of a binning-based inner bone contour extraction, in which all points extracted from each bin (Eq. 5) were connected in an X-ordered manner to form the inner boundary of the bone. The comparison between Fig. 7b and Fig. 9b outlines the effectiveness of binning-based approach in inner contour determination.

As a result of the technique used to select the vertices of the inner boundary, it becomes clear that if the bins are too small/narrow, it is possible that all (both) of its points will be incorrectly placed on the same upper/lower (e.g. anterior/posterior) region of the boundary, which in turn will translate into erroneous contours like the one shown in Fig. 8c. Evidently, the conclusion to be drawn here is that the segmentation method used to generate the preprocessed data will ensure the required variation in point position only if at least three points/bin are enforced. Since the intra-slice sequencing of the points is based on their relative positioning along X direction, rather than on the nearest neighbor approach, this ensures an accurate capturing of all the relevant details of the inner canal geometry, an essential trait for the upcoming implant/bone interference calculations.

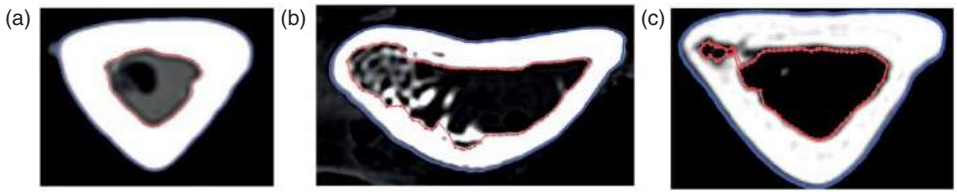

Fig. 10: Sample overlays between raw CT slices and final extracted contours: a) superior match characteristic to medial zone of the humerus, b) approximated inner contours characteristic to distal humerus, and c) special/non-characteristic cases of inner canal configuration.

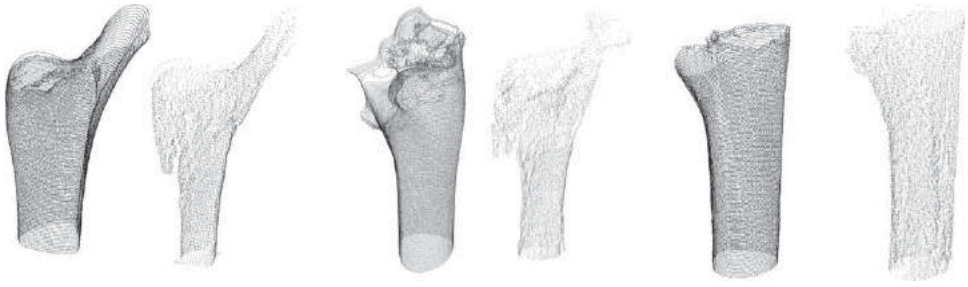

Fig. 11: Final outer (left) and inner (right) contours for three different humeral specimens.

2.4. Generation of Complete Representations for Humeral Specimens

The overlay of sample raw CT images with outer and inner bone contours extracted through the techniques detailed in Sections 2.2 and 2.3 suggests that – in general – an adequate match exists between them. Clearly, the non-homogeneity of the cortical structure along with the geometric complexity of the endosteal canal still pose challenges when attempting to identify the three principal zones of the humeral cross section (Fig. 10).

It is important to emphasize that while superior matches between CT and extracted bone contours generally exist in the medial region of the humerus (Fig. 10a), special cases might also be occur as a result of particular cortical structure (Fig. 10c). However, the local effect of inner contour "necking" will likely be minimal on the implant-bone interference amount since the stem is typically positioned centrally with respect to the endosteal canal in order to allow a good alignment between native and prosthetic FE axes. Similarly, the approximation of the inner canal walls that is characteristic to distal humerus where cancellous/trabecular structure is more frequent is not expected to confound much the interference results since most of the prominences are not captured by the extracted discrete contour. This is in fact in agreement with the experimental observation that most of the trabeculae tend to be crushed anyway during implant insertion procedure.

The application of the developed techniques for outer/inner contour extraction has resulted in specific point-based representations for each of the three analyzed humeral specimens (Fig. 11). Although none of the conventional shading/rendering techniques that are currently available in CAD are capable to provide sufficient cues for an unambiguous visualization of the point datasets/clouds of points, a throughout examination of the three presented samples will reveal – at least in part – the anatomical variability that is inherent to many of the human skeletal components. In all three specimens, the distal zone of the bone was removed to preserve the similarity with the surgical procedure.

3. DETERMINATION OF MAXIMUM INTERFERENCE AMOUNT

For a certain position and orientation of the implant, the amount of interference between stem and humerus can be established based on their relative position. Once the geometry of the humerus is known, determination of the interference amount in each of its planar slices comes down to identification of the interference status for each of the implant points (e.g. non-interfering, interfering and penetration), to be followed by the calculation of the distance with respect to inner canal points, whenever necessary (i.e. interference/penetration is detected).

3.1. Characterization of Implant Posture

Since the type of humeral implants used in the current study is characterized by a fairly simple shape of its stem whose shape is bounded by planar faces, its entire geometry can be described based on the location of 24 characteristic vertices $V_j^i (i, j \in \mathbb{N}, i \leq 3, j \leq 8,)$ located in three different planes: upper ($i = 1$), intermediate ($i = 2$) and lower ($i = 3$) (Fig. 13a). Appropriate pairs of vertices V_j^i and V_j^{i+1} define the 16

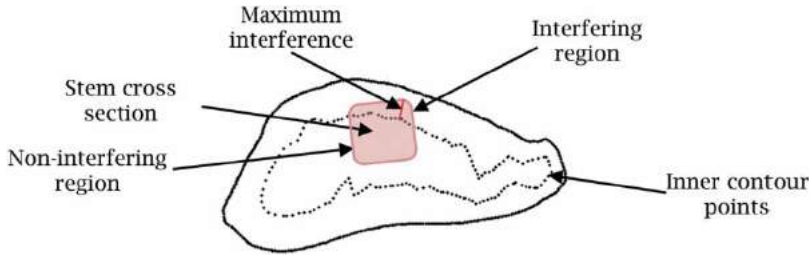

Fig. 12: Determination of maximum interference amount in a planar slice.

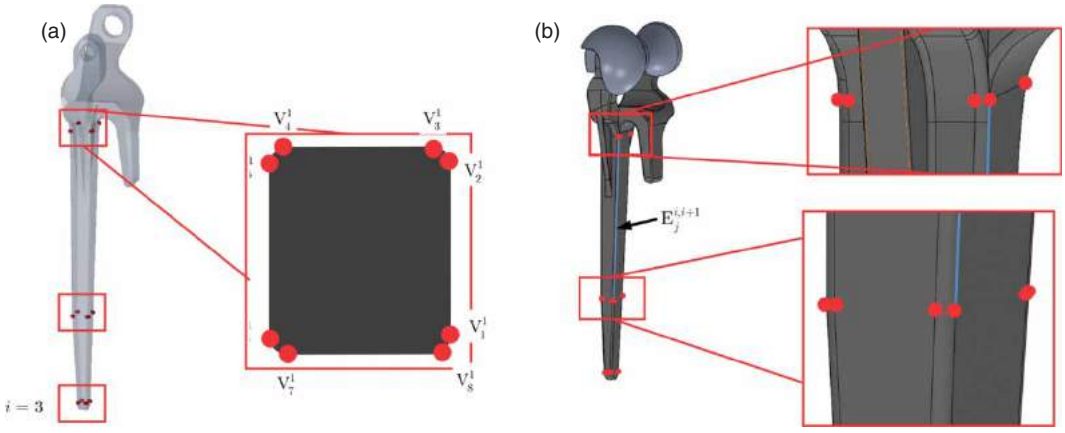

Fig. 13: Significant geometric elements for implant stem: a) characteristic vertices, and b) characteristic edges.

characteristic edges $E_j^{i,i+1}(i,j \in \mathbb{N}, i \leq 2, j \leq 8,)$ that in turn delimit the 8 faces of the stem geometry.

Evidently, for a certain implant type the geometric definition of the characteristic vertices and edges is preset and can be obtained through a direct interrogation of the solid model. Furthermore, all points located along the characteristic edges can be determined with the known parametric relation:

$$\mathbf{P}_{E_j^{i,i+1}} = \mathbf{P}_{V_j^i} + u \cdot (\mathbf{P}_{V_j^{i+1}} - \mathbf{P}_{V_j^i}) \text{ with } u \in [0, 1] \quad (6)$$

It is important to emphasize here that all extracted vertex coordinates are dependent on two main parameters inherently associated with the aforementioned solid model namely: coordinate system and implant posture. In the context of the present study, implant posture ($\mathbf{\Omega}_I$) is defined as the 6D vector obtained through the concatenation of the 3D vectors of associated with its position ($\mathbf{P}_I$) and orientation ($\mathbf{O}_I$), since this information is sufficient to describe the general (e.g. combined translation and rotation) motion of a rigid body:

$$\mathbf{\Omega}_I = [\mathbf{P}_I \quad \mathbf{O}_I] \quad (7)$$

To enable precise determinations of the amount of interference per slice, all points of the implant stem had to be converted into the fixed humeral coordinate system (HCS), the one attached to the bone (Fig. 14a). The axes of this coordinate system were established during by the CT scanner and then kept throughout the subsequent data processing stages. In terms of the actual definitions, X_H and Y_H were contained within the planar slices, while Z_H direction was established by enforcing a certain degree of parallelism between main scanning direction and medullary canal. The origin of HCS was set in the capitellum center of the humerus. On the other hand, the implant data was provided with respect to its own implant coordinate system (ICS) as illustrated by Fig. 14b. Similarly to HCS, the origin of ICS was set in the center of the prosthetic capitellum. The superscript "orig" in the figure corresponds to the original orientation of the ICS, and it was later dropped once the correspondence between ICS and HCS was established. This transformation between the two coordinate systems was acquired by simply overlapping the two FE axes, a transformation performed by means of a rotation with α_{IH} angle about a vector $\hat{\mathbf{n}}_{IH}(\hat{\mathbf{n}}_{IH} = \hat{\mathbf{n}}_{FE_I}^{orig} \times \hat{\mathbf{n}}_{FE_H})$ as shown in Fig. 14c. One of this results of this transformation is that the two FE axes will overlap ($\hat{\mathbf{n}}_{FE_I} = \hat{\mathbf{n}}_{FE_H}$).

The rationale behind this particular type of coordinate transformation resides in the intent to simplify as much as possible the subsequent computational phases by enforcing the quantification of the implant posture with respect to an ideal case of perfect alignment between native and prosthetic FE axes. By doing this, all translational and rotational motions that are determinant for implant posture would represent nothing but direct measurements of the implant

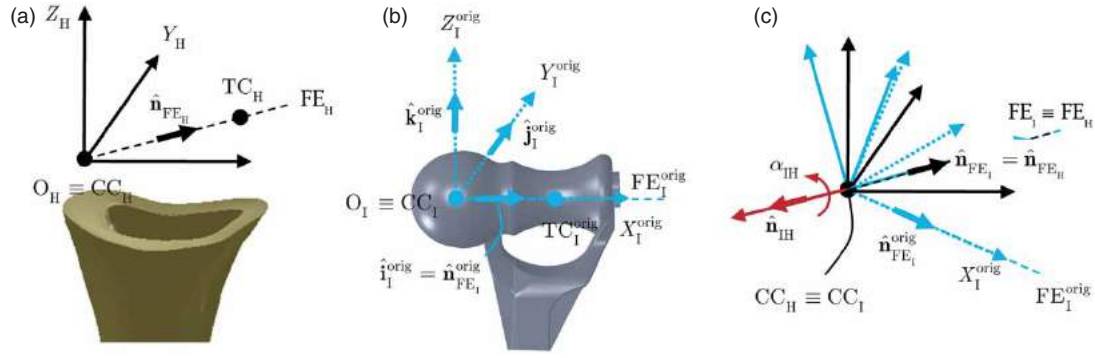

Fig. 14: Coordinate transformation from implant to humeral coordinate system: a) humeral coordinate system, b) implant coordinate system, and c) rotation to overlap native and implant FE axes.

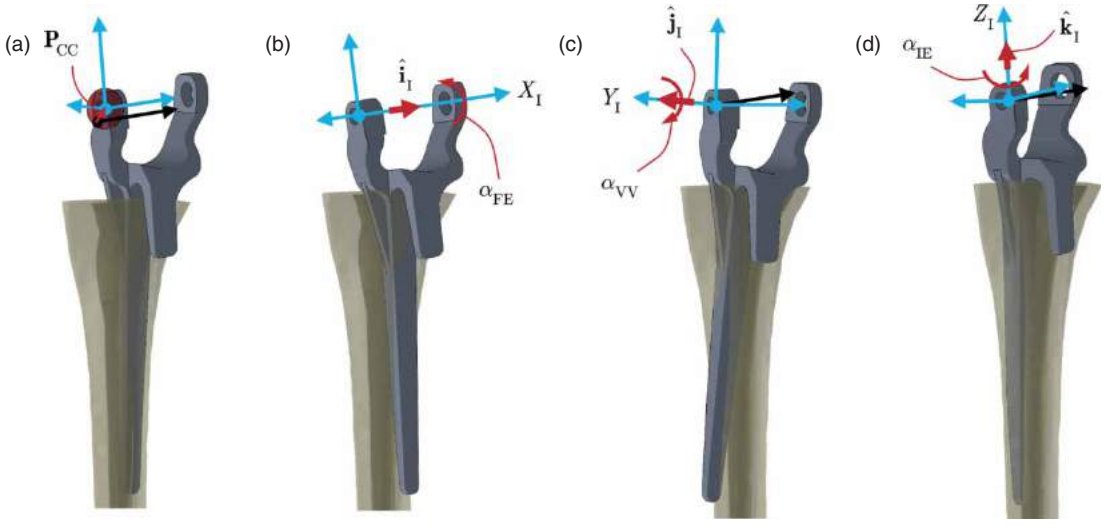

Fig. 15: Characteristic elements of the implant posture: a) capitellar translation, b) flexion extension angle, c) varus-valgus angle, and d) internal-external angle.

malalignment. However, since the standard clinical definition of the malalignment does not include rotation of the implant about the FE axis itself, the initial orientation of the implant was chosen to roughly follow the canal by enforcing the parallelism between the longitudinal axis of the stem and a line determined by the centroids of two arbitrarily selected humeral slices. A more accurate determination of the initial stem orientation is not necessary because for the wide majority of bone-implant pairs the interference free conditions are not attainable anyway when FE axes are perfectly aligned. As such, no major differences would exist between the initial poses of the stem, to serve just as initialization parameters in the upcoming optimization algorithms.

Furthermore, to facilitate the clinical interpretation of the results, the modified implant posture was quantified directly in terms of malalignment between between native and prosthetic FE axes, to translate in positional and angular variations (Fig. 15). A total of six scalar components were used to characterize the instantaneous implant posture with respect to the initial pose obtained immediately the rotation meant to ensure FE axes coincidence:

$$\mathbf{\Omega}_I = [X_{CC} \quad Y_{CC} \quad Z_{CC} \quad \alpha_{FE} \quad \alpha_{VV} \quad \alpha_{IE}] \tag{8}$$

In Eq. (8) X_{CC}, Y_{CC}, Z_{CC} are the three components of the translation between native (CC_H) and prosthetic (CC_I) centers of the capitellum and α_{FE}, α_{VV} and α_{IE} represent flexion-extension, varus-valgus and internal-extension angles, respectively. As Fig. 15b–d indicates, the three rotations were defined with respect to the three axis of the ICS obtained after the α_{IH} rotation, as follows: FE rotation was defined about X_I(α_{FE} angle), VV rotation was defined about Y_I(α_{VV} angle) and IE rotation was defined about Z_I(α_{IE} angle).

As a result, the transformed (e.g. translated and/or rotated) posture of the implant can be expressed through standard homogeneous coordinate transformations controlled by the matrix:

$$\mathbf{T}_{\Omega_I} = \mathbf{R}_{\hat{\mathbf{k}}_I}(\alpha_{IE}) \cdot \mathbf{R}_{\hat{\mathbf{j}}_I}(\alpha_{VV}) \cdot \mathbf{R}_{\hat{\mathbf{i}}_I}(\alpha_{FE}) \cdot \mathbf{T}(\mathbf{P}_{CC}) \cdot \mathbf{R}_{\hat{\mathbf{n}}_{IH}}(\alpha_{IH}) \tag{9}$$

The general coordinate transformation matrix $\mathbf{T}_{\Omega_I}$ enables calculation of the transformed position for any of the vertices of the implant as a function of the implant posture:

$$\mathbf{P}_V^{\text{transformed}} = \mathbf{T}_{\Omega_I} \cdot \mathbf{P}_V^{\text{initial}} \tag{10}$$

Here, the initial coordinates of the implant vertices $\mathbf{P}_V^{\text{initial}}$ were determined based on the aforementioned query of a specific implant model. Through recursive applications of the Eq. (10), the location of all 24 characteristic vertices of the implant can be determined as a function of implant posture. For detailed formulation of the coordinate transformation matrices, the reader is referred to standard CAD/CAM textbooks, like for instance [27].

3.2. Calculation of the Interference Amount

Since the position of the implant vertices and edges changes continuously as a function of the implant posture, it can be inferred that interference is also dependent on the six scalars outlined in Eq. (8). To quantify the total amount of interference between implant and bone (Δ), a metric has been defined as follows:

$$\Delta = \sum_{s=1}^{n_S} \delta_s \tag{11}$$

where δ_i represents the maximum amount of interference existent in slice s while n_S is the number of slices in which interference is possible (stem length is smaller than that of the humerus).

For each of the bone slices located within the possible interference range ($s \in \mathbb{N}, s \leq n_S$), their intersection with 8 of the 16 characteristic edges of the implant was evaluated in order to determine the relative position of the implant cross section with respect to outer/inner contours of the analyzed slice. The calculation of the intersection points involves coupling of Eqs. (6), (9) and (10), such that:

$$\begin{cases} \mathbf{P}_E^{\text{transformed}} = \mathbf{T}_{\Omega_I} \cdot \mathbf{P}_E^{\text{initial}} \\ Z_S = d \end{cases} \tag{12}$$

yields the coordinates of the 8 intersection points between the characteristic edges and the plane of the slice S_s positioned at distance d from the most distal one defined by $s = 1$ and $Z_s = 0$. Hence:

$$P_{S_j} = \{P \in S_s | P = (E_j^{i,i+1})^{\text{transformed}} \cap S_s, i, j \in \mathbb{N}, \\ i \leq 2, j \leq 8\} \tag{13}$$

which implies that $Z_{S_j} = d$. Once the intersection points per slice are known, the interference status for each of them can be determined based on well established algorithms capable to determine the relative position between a point and a polygon [9]. If the outer and inner contour polygons are denoted by $\mathcal{P}_{\mathcal{O}_C}$ and $\mathcal{P}_{\mathcal{I}_C}$ respectively then the maximum amount of interference per slice will be given by:

$$\delta_s = \max(|\mathbf{P}_{P_{S_j}} - \mathbf{P}_{P_{S_j}^C}|), j \in \mathbb{N}, j \leq 8 \tag{14}$$

where $P_{S_j}^C \in \mathcal{I}_C$ represents the closest inner boundary point to P_{S_j}. As a supplementary condition to be met, P_{S_j} is a valid interference point only if $P_{S_j} \notin \mathcal{P}_{\mathcal{I}_C}$. For practical implementation purposes, the same nearest neighbor technique described at Section 2.2 was used to determine $P_{S_j}^C$.

While from a rather theoretical standpoint it could be argued that the maximum interference per slice might also be attained for a point outside of the investigated subset (P_{S_j}) of implant/bone intersection, it is believed that due to the relative uniformity of the inner walls – especially in the narrower humeral cross sections (e.g. away from the distal end of the bone, see Fig. 10a) thus with a larger probability of interference – maximum interference will occur almost always in one of the eight analyzed points P_{S_j}.

4. MINIMIZATION OF THE INTERFERENCE AMOUNT

4.1. Problem Formulation and Solving

When it comes to the determination of the optimal position in which the implant should be positioned inside of the humeral canal for implantation purposes, most orthopaedic surgeons will attempt to minimize the overall amount of cortical bone to be removed since this will diminish the long term durability of the prosthesis. From the perspective of the current work, the amount of bone to be removed is directly proportional with the global interference metric Δ outlined in Eq. (11). Since, as shown in Eqs. (12) and (13), the amount of interference per slice is dependent on the instantaneous position of the stem, it can be inferred that:

$$\Delta = \Delta(\mathbf{\Omega}_I) \tag{15}$$

Eq. (15) quantifies the link between the total amount of interference and implant posture/malalignment. Based on this, the problem at hand is equivalent to determination of $\Delta_{\min}$, where:

$$\begin{cases} \Delta_{\min} = \underset{\Omega_I}{\text{minimize}}(\Delta) \\ 0 \leq |\mathbf{P}_{CC}| \leq d_{\max} \\ \alpha_{FE_{\min}} \leq \alpha_{FE} \leq \alpha_{FE_{\max}} \\ \alpha_{VV_{\min}} \leq \alpha_{VV} \leq \alpha_{VV_{\max}} \\ \alpha_{IE_{\min}} \leq \alpha_{IE} \leq \alpha_{IE_{\max}} \end{cases} \tag{16}$$

As it can be noticed, the 3D translation vector was converted to a more concise magnitude constraint, primarily to preserve a higher clinical relevance of the results. For practical implementation purposes, the

	Implant Position			Implant Orientation		
Input Parameter	r[mm]	θ[°]	ϕ[°]	α_{FE}[°]	α_{VV}[°]	α_{IE}[°]
Lower bound	0	0	−180	−5	−5	−5
Upper Bound	5	180	180	5	5	5
Increment	1	45	45	1	1	1
Total values	6	5	8	11	11	11

Tab. 1: Grid of input parameters used for "brute force" search.

three Cartezian components of $\mathbf{P}_{CC}$ were converted to spherical coordinates (r, θ, φ) that were also easier to constrain numerically.

As Eq. (16) suggests, in order to determine the minimum interference amount, bounds have to be set for each of the six parameters encompassed by the implant posture. Since the surveyed medical literature has proved to be characterized by a relative paucity of information in this regard – most likely due to the technological complications associated with *in-vivo* measurements – somewhat arbitrary limits were chosen for each of the six variables, specifically:

$$\begin{cases} d_{\max} = 5\,\text{mm} \\ \alpha_{FE_{\min}} = \alpha_{VV_{\min}} = \alpha_{IE_{\min}} = -5^\circ \\ \alpha_{FE_{\max}} = \alpha_{VV_{\max}} = \alpha_{IE_{\max}} = 5^\circ \end{cases} \tag{17}$$

The primary rationale behind these numbers was to not exceed too much the range of feasible malalignment values characterized by rather small positional and angular errors.

The problem defined in Eq. (16) represents a classical problem of constrained nonlinear optimization for which an out-of-the-box gradient-based solver [14] was used since both objective and constraints – although highly nonlinear – were characterized by continuous first derivatives. To eliminate or at least diminish the relative confounding of the solution on the initial guess point, a global search solver was used on top of the local gradient-based one. In this regard, global search will run first the local solver from the initial starting point. Once it converges, the global solver will estimate the radius of a basin of attraction from the initial and converging point. A randomized initial set of trial points within the constraints will be then generated and local solver will evaluate where these set of points converge to. Once these points seems to converge reasonably well, a comparative analysis is performed to determine whether the converged point is a local or a global minimum in the test space [6,13,14,22,26].

In addition to global search, a "brute force" search technique was used to determine the minimum interference amount, primarily for comparison and reference purposes. Given the strong dependence of the optimization solution on the initial guess value, a 6D array of initial guess points was dispersed in the posture space according to scheme shown in Tab. 1. As mentioned at Section 4.1, the $\mathbf{P}_{CC}$ translational distance between the two capitella has been mapped into the spherical space for facilitate the enforcement of clinically-relevant bounds. The graphical interpretation of the two angles and distance used to define $\mathbf{P}_{CC}$ is provided in Fig. 16.

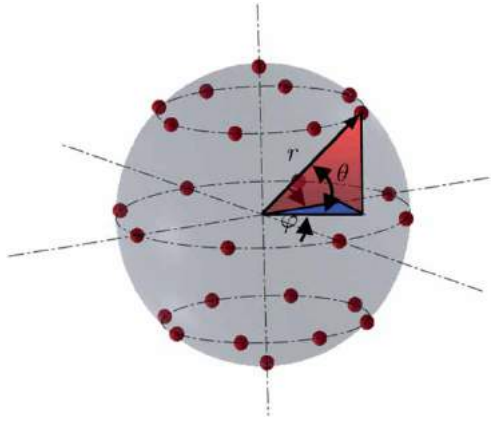

Fig. 16: Discretized spherical coordinates of the 3D space used to quantify "cap-to-cap" translation: r (distance), θ (zenith angle), φ (azimuth angle).

Since the total number of discretized guess points for each of the 6 spheres of variable radius $(0, 1, \ldots, 6)$ analyzed was 26 $(= 8 \times 3 + 2$ poles), the total number of scenarios/initial guess points solved through the "brute force" approach yields at 207,636 $(= 6 \times 26 \times 11 \times 11 \times 11)$.

4.2. Optimization Start Point

Like any other numerical optimization formulation, the developed approach requires an initial start point of the iterations. In order to provide a valid comparison baseline for optimization, its initial point was set to be the one that is typically targeted by the routine elbow arthoplasty procedure. According to the current practices, the surgeon will typically attempt to position the implant in such a way to match/replicate as close as possible the native FE axis of the articulation. As it can be inferred, this "forced" match between the native and prosthetic axes will place the implant and bone in an interference condition as shown in Fig. 17.

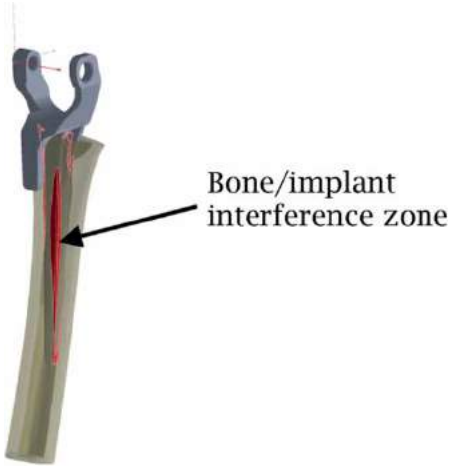

Fig. 17: Initial interference condition at forced bone/implant FE axis alignment.

The quantification of the initial interference conditions for each of the three specimens analyzed is shown in Tab. 2. It is relatively easy to understand that if the requirements for FE axis alignment are relaxed (at least to some extent), the amount of interference can be reduced and this in turn will have positive effects on the amount of cortical to be removed in order to allow implant insertion. The actual results of this iterative process constitute the topic of the next section.

4.3. Results and Discussion

A synthesis of the optimization results obtained through the two solving techniques is provided in Tab. 3. Regardless of the approach used, a simple comparison of the minimized interferences reported in Tab. 2 and 3 will reveal that implant malalignment inevitably translates into a reduced interference between bone and implant stem. Beyond this observation, significant differences are visible between the two analyzed solving techniques. The lower (better) interference values obtained through global search are likely an indication that this method is more precise and thereby superior to "brute force", but not only in terms of runtime. Of course, the high nonlinearity of the problem makes the attainment of identical (or close) results through both numerical solving approaches virtually impossible. However, although the results differ in terms of final objective function, a certain consistency can be noticed among final posture values, especially in the sense that in most scenarios the algorithm stopped because the bound for one of the input variables (generally the same) was reached through both solving techniques. This could be regarded as a positive indication on the correctness and/or robustness of the approach.

Furthermore, since most of the bounds reached were angular, it can be inferred that for TEA, rotational malalignments seem to be more restrictive than the translational ones. While arguably some of the bounds could be loosened to achieve smaller interference values (like, for instance α_{FE} that does not have a direct impact on the malalignment), it can be noticed that the final "cap-to-cap" distances are already somewhere to the upper limit of the clinically acceptable range and therefore their further expansion might not be desirable.

Interestingly, the three specimens tested suggest that the minimum interference free position can be

	Implant Position			Implant Orientation			
Sample No.	X_{CC} [mm]	Y_{CC}[mm]	Z_{CC} [mm]	α_{FE} [°]	α_{VV} [°]	α_{IE} [°]	Δ_{min} [mm]
1	0	0	0	0.2380	0	0	110
2	0	0	0	−5.6105	0	0	450
3	0	0	0	−6.1328	0	0	275

Tab. 2: Summary of minimized interference at initial implant postures.

		Implant Position			Implant Orientation				
Sample No.	Optimization Algorithm	X_{CC} [mm]	Y_{CC} [mm]	Z_{CC} [mm]	α_{FE} [°]	α_{VV} [°]	α_{IE} [°]	Δ_{min} [mm]	Solving Time [min]
1	"Brute force"	0.00	0.00	5.00	−4.00	2.00	−1.00	50.96	1,260
	Global search	−1.68	−0.36	4.69	−5.00	0.33	−1.43	39.62	57
2	"Brute force"	−4.00	0.00	0.00	−5.00	2.00	−5.00	3.58	2,052
	Global search	−4.14	0.00	0.33	−5.00	1.82	−5.00	3.40	17
3	"Brute force"	1.50	−1.50	−2.12	−3.00	−5.00	−5.00	0.00	1,285
	Global search	0.52	−0.59	−0.66	−0.77	−5.00	−5.00	0.00	36

Tab. 3: Summary of minimized interference at final implant postures.

reached in a variety of ways for each of the humeral specimens. These could involve: i) a primarily upward translational motion (essentially similar to implant extraction motion) for specimen 1 (definitely the one with the most challenging implantation/implant fit problem), ii) a primarily anterior/posterior translational motion combined with maximized angular variations for specimen 2, and iii) a minimal translational motion combined with maximized angular malalignment. The values in Tab. 3 also indicate that a broad range of interference values could be encountered in clinical practice. The nil interference observed for specimen 3 simply means that an interference free posture was detected by the solver. However, whether the implant malalignment that is necessary to attain the predicted minimum interference value is acceptable or not from a clinical perspective, it remains to be determined through more appropriate experimental-oriented studies. This observation remains in fact valid for all specimens to be analyzed through the proposed approach.

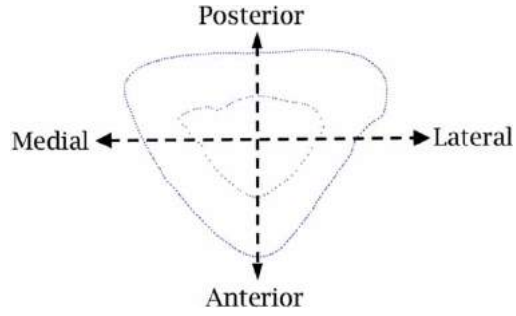

Fig. 18: Principal anatomical directions with respect to cross section.

4.4. Clinically-relevant Results

While all numerical results and comments presented in Section 4.3 have their own clinical implications, it is logical to postulate that orthopaedic surgeons would be interested to know – *prior* to the actual surgical procedure – what are the areas of the humeral bone

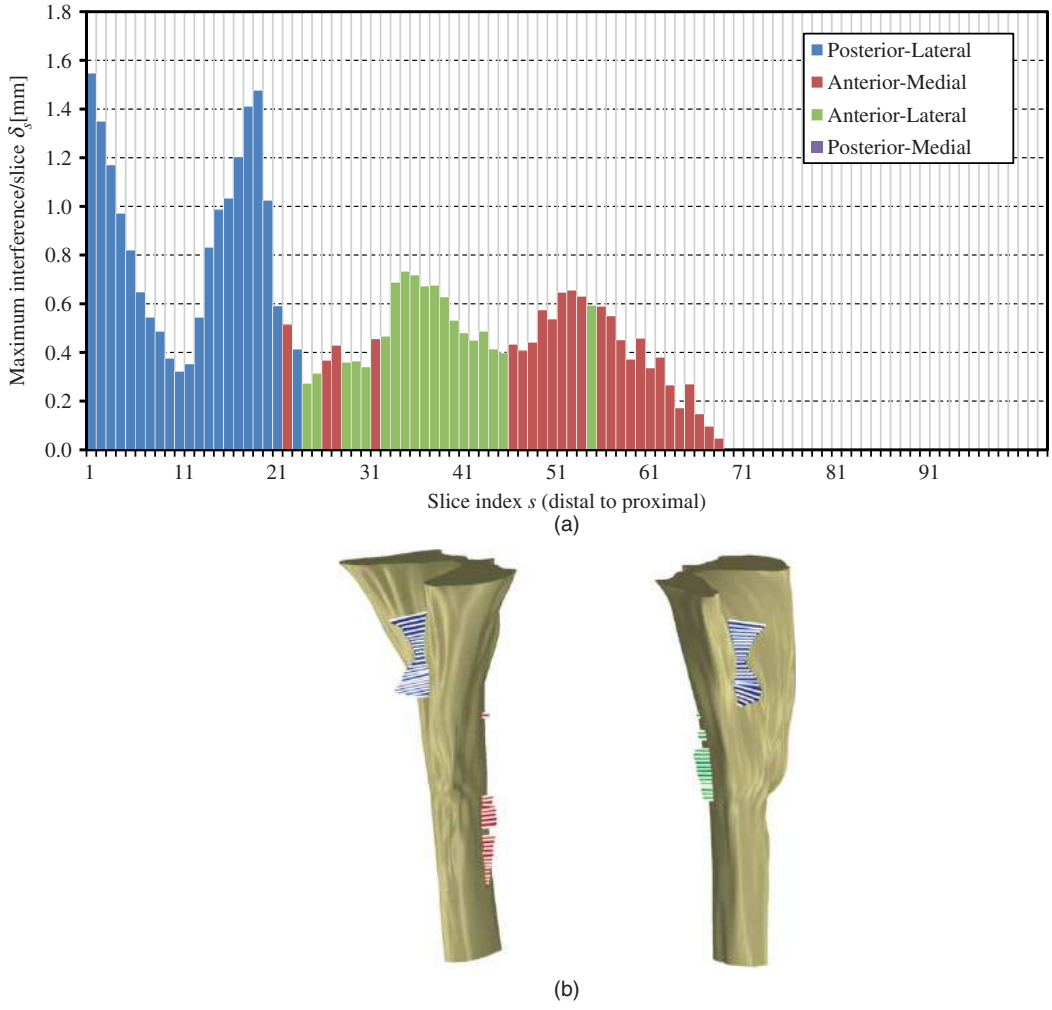

Fig. 19: Variation of the maximum interference amount per slice: a) numerical values and anatomical position, and b) 3D positioning of the interference (exaggerated scale) with respect to inner canal surface.

that are most likely to require cortical bone removal in order to allow implant insertion and fit. To enable further guidance on the anatomical location of the interference point, each humeral cross section was subdivided in four main regions according to the standard anatomical planes (Fig. 18) and the common intersection point of the regions was assumed the centroid of each bone cross section.

To address more directly the clinical needs, Fig. 19a outlines the amount of interference per slice (δ_s) as determined through the developed approach for humeral specimen 1 ("brute force" case). The slice index (s) runs in a distal to proximal direction, slice 1 corresponding to the plane used for osteotomy/excision of the distal humerus as shown in Fig. 2b. The relative positioning of each slice in Cartesian coordinates can be determined based on the CT voxel size, which for in this case was set to 0.625 mm. As the graph suggests, the minimum interference position identified in Tab. 3 translates at slice level into a highly variable amount of interference per slice as well as a variable anatomical localization on the surface of the endosteal canal.

It is realistic to believe that the real amounts of bone to be removed might be different than those suggested by Fig. 19a due to a variety of errors propagated in the process even from the early imaging phases. However, this type of information could serve at least as a qualitative guide to replace the current "blind" or "semi-blind" approach currently used in the surgical practice. Moreover, although the precision of the developed technique could be questioned with respect to the its physical counterpart, it is worth to be mentioned here that – even for the case with the largest Δ – the maximum amount of interference per slice was in the "interference" than "penetration" range, since the cortical thickness for the humerus was reported somewhere around 4.4 ± 1.0 mm [24] This observation validates – perhaps indirectly – that the proposed approach is feasible, or at least to a certain extent.

Virtually the same plot as in Fig. 19a, but perhaps in a more suggestive three-dimensional representation is depicted by Fig. 19b. For clarity of the figure purposes, the scale of the maximum interference per slice was exaggerated and inner surface of the canal was represented in a surface form since point datasets are difficult to visualize.

5. CONCLUSIONS

This study proposes a computational framework capable to predict the minimum amount of cortical bone to be removed in order to ensure a successful implantation of the prosthetic device from the perspective of the total elbow arthroplasty. While it is acknowledged that the approach taken might incorporate a number of errors originating from various sources, it is believed that the developed technique has the potential to become an effective tool to be used preoperatively by the medical professionals at least for training and guidance purposes. The successful implementation and deployment of such predictive numerical tools will likely enhance the accuracy of the present surgical procedures that are still performed in a "blind" or "semi-blind" manner when it comes to the amount and/or the location of the cortical bone to be removed from the inner canal of the humerus. This type of knowledge is essential for a superior prosthetic to native FE axis alignment, one of the *sine qua non* conditions of a durable elbow arthroplasty.

Future extensions of this work will attempt integration of supplementary constrains with clinical relevance as well as practical validations/clarifications of some of the uncertainties identified in the current study, most likely related to the clinically allowable ranges for implant posture parameters.

ACKNOWLEDGEMENTS

This work was financed in part by National Sciences and Engineering Research Council of Canada also through a special training program on Computer-Aided Medical Intervention. The authors would like to express their sincere thanks to Dr. James Johnson and Dr. Graham King from Hand and Upper Limb Centre (HULC) in St. Joseph's Health Care, London, Canada for their continuous support and assistance towards this project. The authors would also like to acknowledge Tornier Inc. (Stafford, Texas, USA) for providing of the implant data.

REFERENCES

[1] Browhill, J. R.; Furukawa, K.; Faber, K. J., Johnson, J. A.; King, G. J. W.: Surgeon accuracy in the Selection of the Flexion-Extension Axis of the Elbow: An in Vitro Study, Journal of Shoulder and Elbow Surgery, 15(4), 2006, 451–456. http://dx.doi.org/10.1016/j.jse.2005.09.011

[2] Brownhill, J. R.; Pallock J. W.; Ferreira, L. M.; Johnson, J. A.; King, G. J. W.: The Effect of Implant Malalignment on Joint Loading in Total Elbow Arthroplasty, Journal of Shoulder and Elbow Surgery, 21(8), 2012, 1032–1038. http://dx.doi.org/10.1016/j.jse.2011.05.024

[3] Chafik, D.; Gupta, R.: Primary Total Elbow Arthroplasty, Operative Techniques in Orthopaedics, 12(1), 2002, 15–20. http://dx.doi.org/10.1053/otor.2002.34441

[4] Chapman, M.: The Effect of Reamed and Nonreamed Intramedullary Nailing on Fracture Healing, Clinical Orthopaedics and Related Research, 355S, 1998, S230–S238. http://dx.doi.org/10.1097/00003086-199810001-00023

[5] Fevang, B. T. S.; Lie, S. A.; Havelin, L. I.; Skrederstuen, A.; Furnes, O.: Results after 562 Total

Elbow Replacements: A Report from the Norwegian Arthroplasty Register, Journal of Shoulder and Elbow Surgery, 18(3), 2009, 449–456. http://dx.doi.org/10.1016/j.jse.2009.02.020

[6] Glover, F.: A Template for Scatter Search and Path Relinking, Artificial Evolution, Lecture Notes in Computer Science 1363, Springer (1998), 13–54. http://dx.doi.org/10.1007/BFb0026589

[7] Gregory, J. J.; Ennis, O.; Hay, S. M.: Total Elbow Arthroplasty, Current Orthopaedics, 22(2), 2008, 80–89. http://dx.doi.org/10.1016/j.cuor.2008.04.008

[8] Ikavalko, M.; Lehto, M. U. K.; Repo, A.; Kautiainen, H.; Hamalainen, M.: The Souter-Strahclyde Elbow Arthroplasty – A Clinical and Radiological Study of 525 Consecutive Cases, The Bone and Joint Journal, 84(1), 77–82. http://dx.doi.org/10.1302/0301-620X.84B1.11848

[9] Hormann, K.; Agathos, A.: The Point in Polygon Problem for Arbitrary Polygons, Computational Geometry, 20(3), 2001, 131–144. http://dx.doi.org/10.1016/S0925-7721(01)00012-8

[10] Kim, J. M.; Mudgal, C. S.; Konopka, J. F.; Jupiter, J. B.: Complications of Total Elbow Arthoplasty, Journal of the American Academy of Orthopaedic Surgeons, 19, 2011, 328–339.

[11] Kitware, Inc.; VTK User's Guide Version 5. Clifton Park, New York, 2006.

[12] Krenek, L.; Farng, E.; Zingmond, D.; SooHoo, N. F.: Complication and Revision Rates Following Total Elbow Arthroplasty, Journal of Hand Surgery, 36(A), 2011, 68–73. http://dx.doi.org/10.1016/j.jhsa.2010.09.036

[13] Lorensen, W. E.: Marching Cubes: A High Resolution 3D Surface Construction Algorithm, Siggraph Proceedings of the 14th annual conference on Computer graphics and interactive techniques, 21(4), 1987, 163–169. http://dx.doi.org/10.1145/37401.37422

[14] MathWorks: Global Optimization Toolbox – User's Guide, Natick, MA, 2012

[15] McDonald, C. P.; Johnson, J. A.; Peters, T. M.; King, G. J. W.: Image-based Navigation Improves the Positioning of the Humeral Component in Total Elbow Arthroplasty, Journal of Shoulder and Elbow Surgery, 19(4), 2010, 533–543. http://dx.doi.org/10.1016/j.jse.2009.10.010

[16] McDonald, C. P.; Peters, C. P.; Johnson, T. M.; King, G. J. W.: Stem Abutment Affects Alignment of the Humeral Component in Computer-assisted Elbow Arthroplasty, Journal of Shoulder and Elbow Surgery, 20(6), 2011, 891–898. http://dx.doi.org/10.1016/j.jse.2010.12.012

[17] McDonald, C. P.: Image-Guided Surface-Based Registration of the Elbow, Library and Archives Canada, London, Ontario, Canada, 2008.

[18] O'Driscoll, S.; Jupiter, J.; King, J. W. G.; Hotchkiss, R. N., Morrey, B. F.: The Unstable Elbow, Journal of Bone and Joint Surgery, 82(5), 2000, 724–724.

[19] O'Driscoll, S.; Yamaguchi, K.; King, G. J. W.: Surgical Technique - Total Elbow Prosthesis - Latitude, Tornier, Montbonnot, France, 2012.

[20] Tutunea-Fatan, O. R.; Bernick, J. H.; Lalone, E.; King, G. J. W.; Johnson, J. A.: Application of Collision Detection to Assess Implant Insertion in Elbow Replacement Surgery, Medical Imaging 2010: Visualization, Image-Guided Procedure, and Modeling, 7625. http://dx.doi.org/10.1117/12.840548

[21] Sabo, M. T.; Athwal, G. S.; King, G. J. W.: Landmarks for Rotational Alignment of the Humeral Component during Elbow Arthroplasty, Journal of Bone and Joint Surgery, 94(A), 1794–1800. http://dx.doi.org/10.2106/JBJS.J.01740

[22] Schaffler, S.: Global Optimization, Springer, New York, 2012. http://dx.doi.org/10.1007/978-1-4614-3927-1

[23] Schuind, F.; O'Driscoll S.; Korinek, S.; An, K. N.; Morrey, B. F.: Loose-hinge Total Elbow Arthroplasty, The Journal of Arthroplasty, 10(5), 1995, 670–678. http://dx.doi.org/10.1016/S0883-5403(05)80214-1

[24] Tingart, M. J.; Apreleva, M.; von Stechow, D., Warner, J. J.: The Cortical Thickeness of the Proximal Humeral Diaphysis Predicts Bone Mineral Density of the Proximal Humerus, Journal of Bone and Joint Surgery, 85(4), 2003, 611–617. http://dx.doi.org/10.1302/0301-620X.85B4.12843

[25] Tsai, M. D.; Hsieh, M. S.; Tsai, C. H.: Bone Drilling Haptic Interaction for Orthopedic Surgical Simulator, Computers in Biology and Medicine, 37(12), 2007, 1709–1718. http://dx.doi.org/10.1016/j.compbiomed.2007.04.006

[26] Ugray, Z.; Lasdon, L.; Plummer, J.; Glover, F.; Kelly, J.; Marti, R.: Scatter Search and Local NLP Solvers: A Multistart Framework for Global Optimization, INFORMS Journal on Computing, 19(3), 2007, 328–340. http://dx.doi.org/10.1287/ijoc.1060.0175

[27] Zeid, I.: Mastering CAD/CAM, McGraw-Hill, New York, NY, USA, 2004.